Full waveform tomographic images of the peak ring at the Chicxulub impact crater

J. V. Morgan,[1] M. R. Warner,[1] G. S. Collins,[1] R. A. F. Grieve,[2] G. L. Christeson,[3] S. P. S. Gulick,[3] and P. J. Barton[4]

[1] Peak rings are a feature of large impact craters on the terrestrial planets and are generally believed to be formed from deeply buried rocks that are uplifted during crater formation. The precise lithology and kinematics of peak ring formation, however, remains unclear. Previous work has revealed a suite of bright inward dipping reflectors beneath the peak ring at the Chicxulub impact crater and that the peak ring was formed from rocks with a relatively low seismic velocity. New two-dimensional, full waveform tomographic velocity images show that the uppermost lithology of the peak ring is formed from a thin (~100–200 m thick) layer of low-velocity (~3000–3200 m/s) rocks. This low-velocity layer is most likely composed of highly porous, allogenic impact breccias. Our models also show that the change in velocity between lithologies within and outside the peak ring is more abrupt than previously realized and occurs close to the location of the dipping reflectors. Across the peak ring, velocity appears to correlate well with predicted shock pressures from a dynamic model of crater formation, where the rocks that form the peak ring originate from an uplifted basement that has been subjected to high shock pressures (10–50 GPa) and lie above downthrown sedimentary rocks that have been subjected to shock pressures of <5 GPa. These observations suggest that low velocities within the peak ring may be related to shock effects and that the dipping reflectors underneath the peak ring might represent the boundary between highly shocked basement and weakly shocked sediments.

Citation: Morgan, J. V., M. R. Warner, G. S. Collins, R. A. F. Grieve, G. L. Christeson, S. P. S. Gulick, and P. J. Barton (2011), Full waveform tomographic images of the peak ring at the Chicxulub impact crater, *J. Geophys. Res.*, *116*, B06303, doi:10.1029/2010JB008015.

1. Background

1.1. Introduction

[2] The Chicxulub impact crater, Mexico, is best known for being linked to the Cretaceous-Paleogene (K-Pg) mass extinction [e.g., *Hildebrand et al.*, 1991; *Schulte et al.*, 2010]. Chicxulub is also one of the largest known craters on Earth, is well preserved and is unique in that it is the only terrestrial crater that clearly possesses an intact (preserved) topographic peak ring. Peak rings are a semicontinuous to continuous topographically high annulus internal to the main crater rim and are a feature of large impact craters on silicate bodies in the solar system (e.g., Figure 1). Seismic reflection images of the peak ring at Chicxulub (Figure 2) show that it is morphologically similar to peak rings on other planetary bodies [*Morgan et al.*, 2000]. Several other terrestrial craters have internal ring-like features (e.g., Vredefort, Popigai, Clearwater West, and Ries craters), which may be related to an original peak ring structure but these structures have been eroded to various degrees and the "rings" at different craters are lithologically and structurally different. As a result, we cannot be unequivocal as to which of these "rings" (if any) are directly analogous to peak rings in large craters on other planetary bodies.

[3] Two-dimensional reflection and three-dimensional traveltime tomographic images of the offshore portion of the peak ring at Chicxulub have revealed a number of interesting features (Figure 2). The peak ring is roughly circular and buried ~600–1000 m below surface [*Gulick et al.*, 2008]. What are interpreted to be postimpact sediments onlap the peak ring [*Bell et al.*, 2004], which suggests it remained as a topographic high for some time after impact. All tomographic velocity models, to date, indicate that the lithologies that form the peak ring have lower seismic velocities than the lithologies immediately adjacent to the peak ring [*Christeson et al.*, 1999; *Morgan et al.*, 2000;

[1]Department of Earth Science and Engineering, Imperial College London, London, UK.
[2]Department of Earth Sciences, University of Western Ontario, London, Ontario, Canada.
[3]Jackson School of Geosciences, University of Texas Institute for Geophysics, Austin, Texas, USA.
[4]Department of Earth Sciences, University of Cambridge, Cambridge, UK.
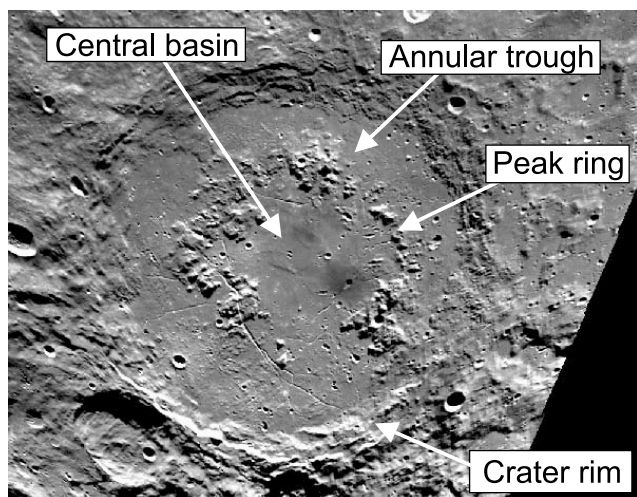
Figure 1. Clementine mission image of the Schrödinger crater, a 321 km diameter peak ring basin on the Moon. The peak ring is a topographic feature, emergent above the allogenic impact deposits that cover the crater floor.

Barton et al., 2010]. The central and inner part of the peak ring correlates with a circular gravity low (colored pink/purple in Figure 3), suggesting that the peak ring is formed from low-density material [*Pilkington et al.*, 1994; *Vermeesch and Morgan*, 2004], in support of the changes in relative seismic velocity.

[4] In the absence of a definitive outcrop of a peak ring in large craters on Earth, our understanding of peak rings has been limited to remote sensed observations of impact craters on other planetary bodies and to the numerical modeling of large crater formation [*Head*, 1977; *Grieve et al.*, 1981; *Bussey and Spudis*, 1997; *Collins et al.*, 2002]. Thus, the exact lithological and structural nature of peak rings is unknown and constitutes a major gap in our understanding of large-scale impact crater formation. Here, we present the results from 2-D full wavefield tomographic inversions of seismic data across the peak ring at Chicxulub. The use of full wavefield techniques is increasing, as they have the potential to resolve variations in seismic velocity at a much higher resolution than is possible with other techniques. We have used our tomographic velocity models to convert migrated reflection stacks from time to depth. In the discussion, we compare our new velocity models with a dynamic model of crater formation and show that velocity across the peak ring appears to correlate with maximum recorded shock pressures due to crater formation.

1.2. Peak Rings

[5] Peak rings possess a distinct morphological character forming an annulus of rugged hills located inside the main topographic crater rim; these hills protrude through the impact melt rocks and breccias within the crater (see Figure 1). On Earth, emergent peak rings do not survive as such for long, as they can be eroded, altered by tectonism, or buried beneath younger postimpact sediments. Internal "rings" within terrestrial craters generally correspond to one of four different elements: structural elements in the parautochthonous lithologies in the crater floor (Vredefort), near-surface rocks that have been overturned (Ries), an expression of strati-

graphic uplift (West Clearwater, Popigai), and the occurrence of megabreccia (Popigai). In all cases, it is unclear whether these elements represent a remnant of a topographic feature in the pristine crater and, hence, whether or not the element is analogous to peak rings, as observed in large extraterrestrial craters. As a result, with the exception of Chicxulub, there is no widely acknowledged or known example of a terrestrial peak ring.

[6] Most models of peak ring formation consider that it is generated during the collapse of a deep bowl-shaped "transient crater" formed during the initial stages of cratering [*Grieve et al.*, 1981; *Melosh*, 1989]. During this collapse, structural uplift of the crater floor produces a central uplift, which is over-heightened and unstable under gravity, and then collapses outward to form a peak ring (e.g., Figures 4a–4c). Numerical models of the formation of the Chicxulub crater have demonstrated that a peak ring can be formed as centrally uplifted material collapses outward [*Morgan et al.*, 2000; *Collins et al.*, 2002; *Ivanov*, 2005, *Senft and Stewart*, 2009]. In these models, material that starts in the uplifted transient cavity rim, collapses downward and inward, while material in the central uplift collapses downward and outward and forms a topographic high, when it collides with the down-thrown transient cavity rim (Figure 4c). It has been proposed that a suite of enigmatic inward dipping reflectors, that are visible on most reflection profiles that cross the peak ring at Chicxulub (e.g., Figure 2b), represent the boundary between these two collapse regimes [*Morgan et al.*, 2000]. Numerical models can replicate the observed geometry of the Chicxulub crater, in particular that down-faulted Cretaceous sediments from the transient cavity rim area lie beneath the outer edge of the peak ring [*Morgan et al.*, 2000; *Collins et al.*, 2002] (see Figures 4 and 5).

[7] Structural observations at the Vredefort and Sudbury impact craters also appear broadly consistent with peak rings formed as material collapses inward and interacts with the outwardly collapsing central uplift [*Grieve et al.*, 2008]. In addition, spectral data from the Moon indicate that central peaks and, in particular, peak rings contain material that has been uplifted from deeper layers in the crust [*Bussey and Spudis*, 1997]. Thus, a range of observational data, supported by numerical models, suggest that peak rings are formed from material that was originally deep below surface, which has been structurally uplifted and then collapsed outward. However, the precise lithologic nature (what does peak ring material comprise) and the detailed kinematics of peak ring formation (from what location does this material derive originally, and how does it reach its final destination) remain unclear.

1.3. Seismic Data

[8] Seismic reflection and refraction data were acquired across the Chicxulub crater in 1996 and 2005 [*Morgan et al.*, 1997; *Gulick et al.*, 2008]. The 2005 data include a dense suite of profiles across the peak ring, which were acquired as part of a site survey for proposed Integrated Ocean Drilling Program (IODP) drilling of the peak ring (Figure 3). These reflection data were acquired using the R/V *Maurice Ewing* with a 20 air gun array of 6947 cubic inches and a 6 km hydrophone streamer with 480 channels. The shot interval was 50 m along each line. The air gun array was towed at 6 m and the streamer at 7 m depth. For lines R3 and
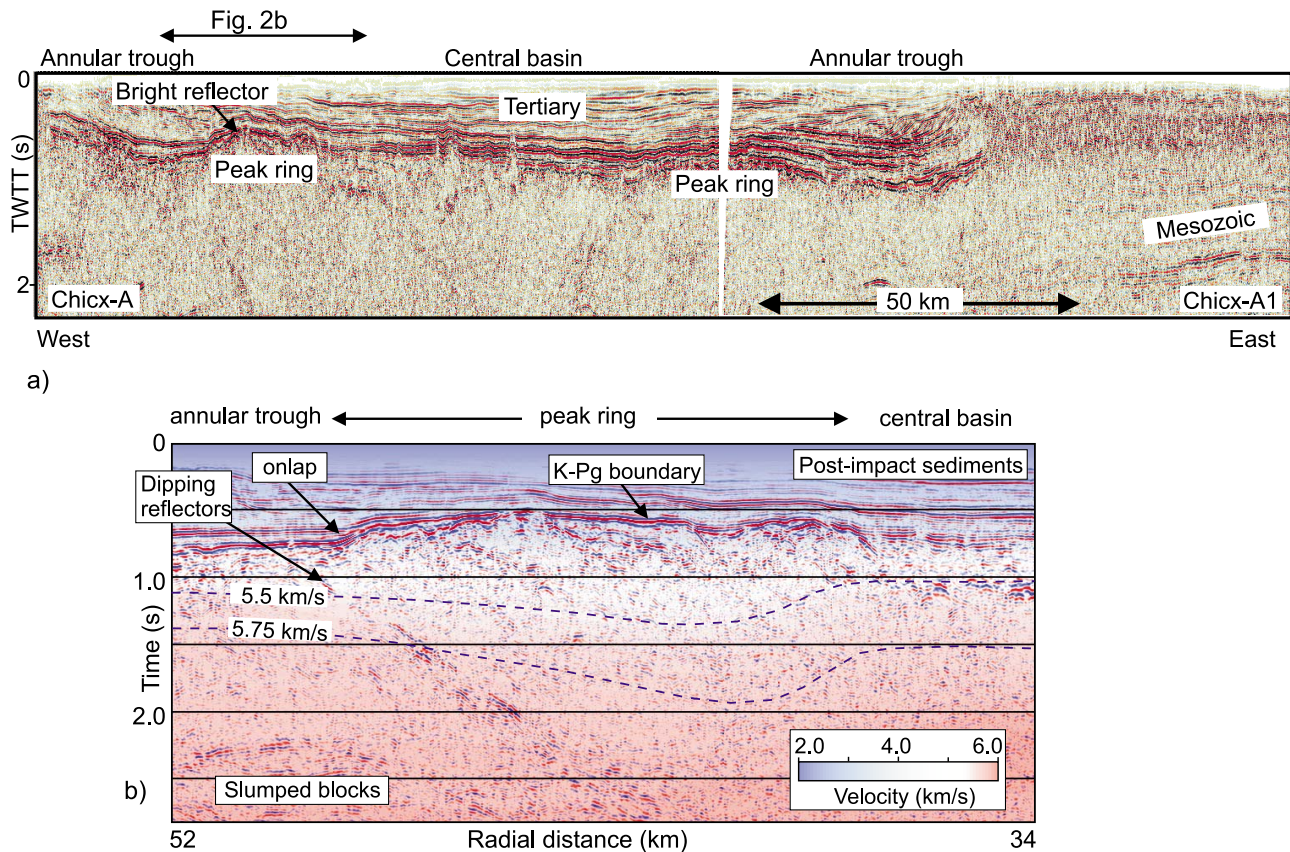
Figure 2. (a) Seismic reflection stack of profile Chicx-A and Chicx-A1 at Chicxulub (see Figure 3 for location). A bright reflector defines the upper surface of the peak ring and marks a change in reflection character between the high-frequency coherent sediments (above) to more sparse and chaotic low-frequency reflections (below). Onshore drill holes were used to interpret this reflector as the K-Pg boundary [*Bell et al.*, 2004]. (b) Reflection stack across the peak ring plotted over a tomographic velocity model [from *Morgan et al.*, 2000]. The surface of the peak ring is hummocky and stands 300–400 m above the K-Pg boundary in the annular trough and central basin. A suite of inward dipping reflectors run from the outer edge of the peak ring. Cretaceous sediments have been tracked from outside the crater, where they are intact and coherent, across a series of faulted blocks (see Figure 5), the innermost of which lies beneath the outer edge of the peak ring. Color is a 3-D traveltime tomographic velocity model (converted from depth to time); contours of constant velocity deepen within the peak ring (in depth as well as in time).

17, the offset to the nearest channel was 112.5 m and, for line 10, it was 180 m. The reflection data were processed at the University of Texas; processing included an F-K filter, an 8 Hz low-cut filter and spectral band-pass whitening [*Gulick et al.*, 2008]. The data were migrated with a poststack Kirchoff migration (maximum dip of 60°), using a smoothed velocity function generated from MCS and refraction data.

[9] Figure 6 shows the migrated stacks of the three reflection lines (R3, 10, 17). All three lines image the annular trough and peak ring, but do not reach the central basin (see Figures 1, 2, and 5 for terminology). The profiles are 20 km long and the same seismic data that were used to generate these stacks are also used for the tomographic inversions described below.

2. Method

[10] In traveltime tomography, we minimize the mismatch between observed and calculated seismic travel times;

whereas, in full waveform tomography we seek a model that is able to match the entire observed wavefield. Hence, in traveltime tomography spatial resolution is limited to about the width of the first Fresnel zone [*Williamson*, 1991] but full wavefield tomography has a resolution of around the seismic wavelength [*Wu and Toksöz*, 1987], which is typically an order of magnitude better than that of traveltime tomography. Here, we use a 2-D frequency domain viscoacoustic code [*Pratt*, 1999] which involves: forward propagation of a source through the current model, subtraction of the predicted and observed data to obtain a residual, backward propagation of the residual through the same model followed by cross correlation of the forward and residual data sets to provide an unscaled model update. A further forward modeling step is required, in order to determine the magnitude of the update, and the velocity model is modified accordingly. This process is iterated to provide a full nonlinear solution. In two dimensions, frequency domain codes have the advantage of being more
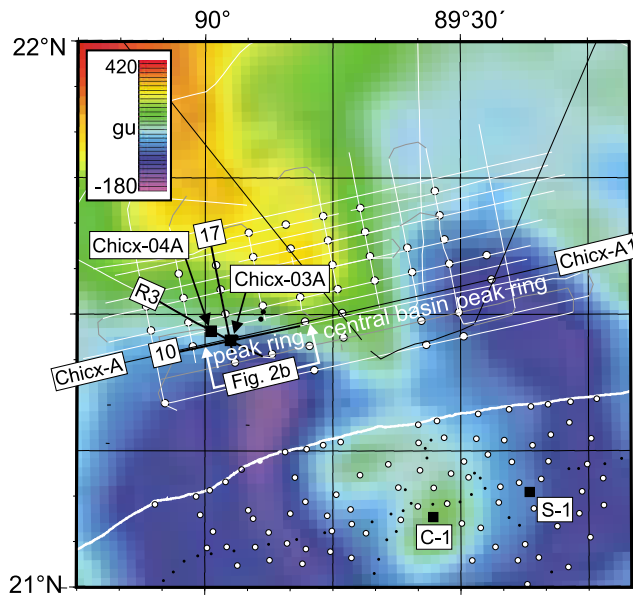
Figure 3. Bouguer gravity image of Chicxulub. Gray and white lines show the location of the offshore reflection profiles acquired in 1996 and 2005, respectively. Dots are the locations of seismometer stations that were used in the traveltime tomographic inversions. Chicx-A and Chicx-A1 are the reflection lines shown in Figure 2, and the location of Figure 2b is labeled. The peak ring and central basin labels show the location of these features in Figures 2a and 5. Black lines locate the parts of reflection profiles R3, 17, and 10 that were used for the full wavefield inversions. Solid black squares show the location of two onshore drill holes, S-1 and C-1, and two planned Integrated Ocean Drilling Program drill holes, Chicx-03A and Chicx-04A. Thick white line shows the location of the coast.

computationally efficient than time domain codes and they also allow the recovery of long-wavelength structure first, through inverting iteratively from low to high frequencies [*Pratt and Worthington*, 1988]. A limitation of the code used here, however, is that it is viscoacoustic and, hence, does not account for the elastic part of the wavefield.

[11] The full wavefield method is dependent upon obtaining a good starting model, which must predict the first-arrival travel times to within half a cycle, at the lowest frequency present (and inverted) in the data [*Sirgue and Pratt*, 2004]. Hence, it is an advantage if low-frequency signals are present in the data, with acceptable signal-to-noise ratios. Some form of preprocessing of the seismic data is often required, which should include removing or reducing the amplitudes of S wave and surface wave arrivals, if they are not modeled by the code. The spacing of grid points, frequencies to invert, and sampling of the input data, must all be chosen carefully in order to avoid aliasing and numerical artifacts [*Brenders and Pratt*, 2007; *Takougang and Calvert*, 2010]. Typically, the inversions are run multiple times to test the effects of different starting models, source wavelets, and different inversion strategies. A commonly used approach is to update upper model structure first by restricting the inversion, and/or time-windowing the data, and/or restricting the data offsets. Deeper parts of the model are then updated by including longer offsets and longer time windows.

[12] In the inversions presented here, starting models for the wavefield inversions were obtained using the traveltime tomographic inversion code, FAST [*Zelt and Barton*, 1998]. The FAST program uses a regularization that leads to a smooth or minimally perturbed velocity model that fits the travel time data to within the pick uncertainty. Smooth starting models are considered to be preferable for full wavefield inversions, as incorrectly placed sharp boundaries will tend to dominate the inversion.

3. Results

[13] An example of a typical shot gather is shown in Figure 7a. An uncertainty of 20 ms was used for all traveltime picks. Travel times for every fourth shot (every 200 m) were picked and input into the FAST inversion. The velocity models are 20 km long by 3 km deep, with a node spacing of 50 m. The starting velocity model for all the traveltime inversions is shown in Figure 8a and was chosen to be consistent with previous tomographic inversions [*Vermeesch and Morgan*, 2008]. In addition, a 1-D starting velocity model is preferential to ensure that all structure in the inverted velocity model is required by the data [*Zelt*, 1999]. A number of different starting models were tested but produced no significant changes in the inverted velocity models. The results of the FAST traveltime inversions are shown in Figures 8b–8d. In FAST, there are two free parameters (α and s_z) that are used to regularize the inversion and, for the inversions shown in Figure 8, these were set to obtain a smooth velocity model ($\alpha = 0.9$), with smoothness in the horizontal direction being more heavily weighted than in the vertical ($s_z = 0.2$) [see *Zelt and Barton*, 1998]. All three inverted models fit the first-arrival travel times well with a χ^2 of close to 1. These velocity models were then used as the input starting models for the full wavefield inversions.

[14] For the full wavefield inversions, three different sources were tested. These were: (1) derived statistically from the data, assuming a minimum phase, (2) obtained from a near offset stack, and (3) constructed from the known source and receiver geometries. In addition, the inversions were run multiple times with different preprocessing applied to the input data, to test the effects of different filters, time-windowing of the data and weighting of the data amplitudes on inversion results.

[15] Results from the full wavefield inversions are shown in Figure 9. For these inversions, five frequencies were inverted (5, 6, 7, 8, 10 Hz), the node spacing in the velocity models was 12.5 m and the sampling interval for the seismic data was 4 ms. At each of these frequencies, the misfit reduction was between 40 and 60%. Inversions using frequencies of 12 Hz and above led to a minimal reduction in misfit (<20%). The poor performance at higher frequencies occurs because wavefield inversions are nonlinear and nonlinearity increases with increasing frequency, owing to accumulated inaccuracies in the inverted velocity model at lower wave numbers [*Sirgue*, 2003]. This means that wavefield inversions in the frequency domain typically start at low frequencies and stop at frequencies of between 7 and 12 Hz [e.g., *Brenders and Pratt*, 2007; *Sirgue et al.*, 2010;
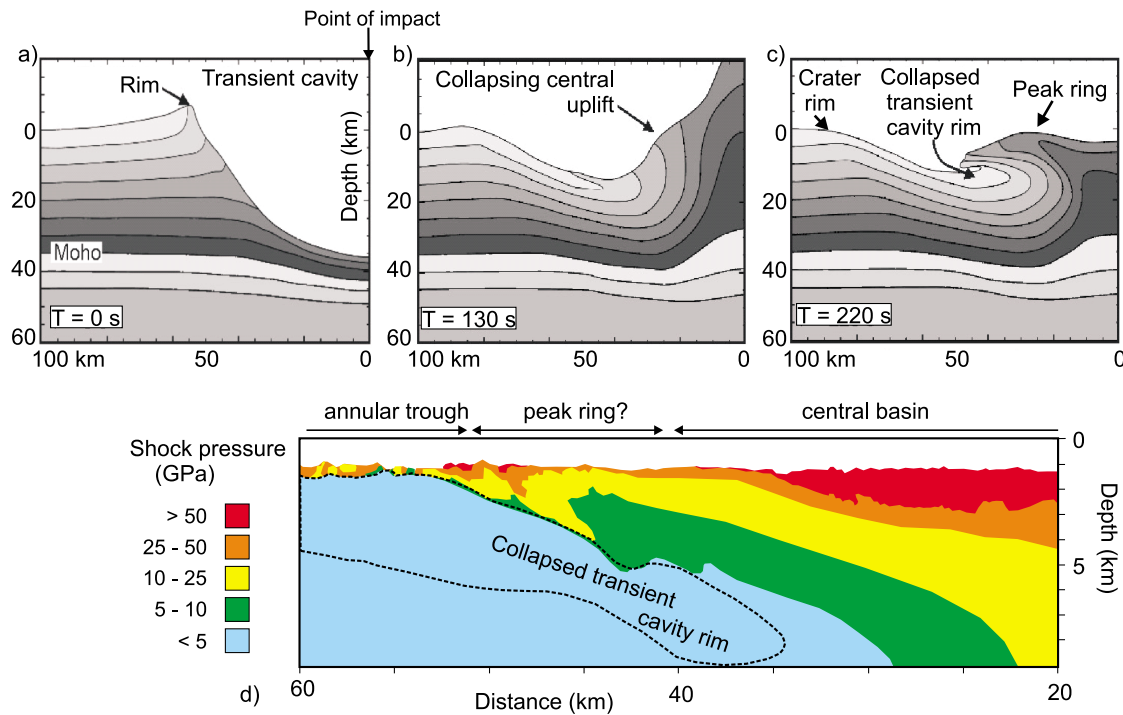
Figure 4. Hydrocode simulation of the formation of the Chicxulub crater [from *Morgan et al.*, 2000; *Collins et al.*, 2002, 2008a]. Layering shows stratigraphy; impact point and center of crater are at a horizontal distance of 0 km. Sediments that form (a) the transient cavity rim collapse inward and downward, while (b) material in the central crater collapsed upward. (c) In this model the stratigraphically uplifted material (central uplift) collapses outward across the downthrown rim material to form a peak ring. (d) Cross section through the final crater. Color shows maximum shock pressures that rocks have been subjected to during crater formation. Dashed line shows the location of sediments that originally formed the transient cavity rim (see Figure 4a).

Takougang and Calvert, 2011]. A source derived from a stack of near-offset data was used for all the inverted velocity models in Figure 9 (see insert in Figure 7b) but the tested alternative sources produced a negligible effect on the final models. The shallow water layer (~15 m) was not included in the velocity model as the traveltime difference between sediments and water is small, but the effect of the water layer was added to the source in the forward calculation of
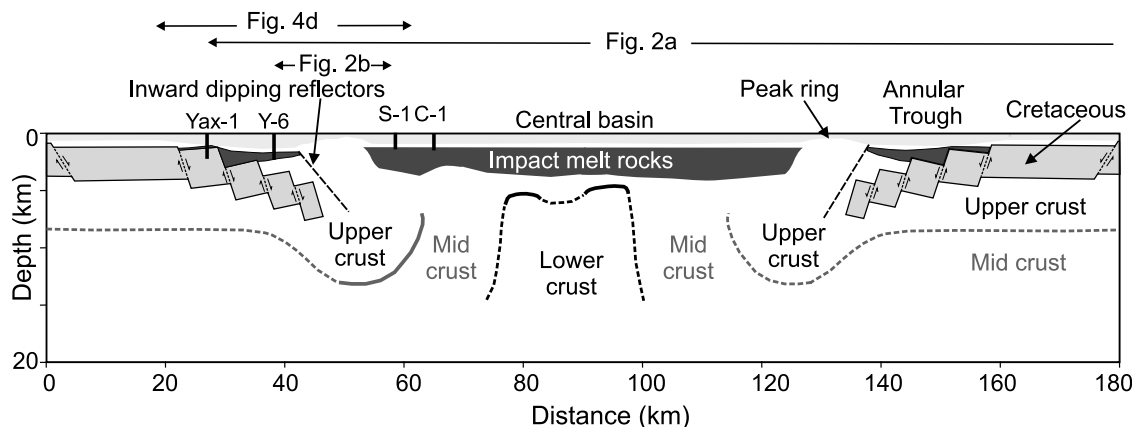

Figure 5. Model of the Chicxulub crater, which is consistent with drill core and geophysical data [from *Vermeesch and Morgan*, 2008]. Onshore drill holes S-1, C-1, Y-6, and Yax-1 were drilled in the central basin and annular trough (see Figure 3 for location). The locations of the lower crust, middle crust, and upper crust are derived from velocity models obtained using 3-D joint density and traveltime inversions, and solid lines show areas that are well constrained. The peak ring is left unlabeled, as it is not clear where the rocks that form the peak ring are derived, and numerical simulations (Figure 4) suggest that they may comprise overturned sediments, upper crust, middle crust, or even lower crust.
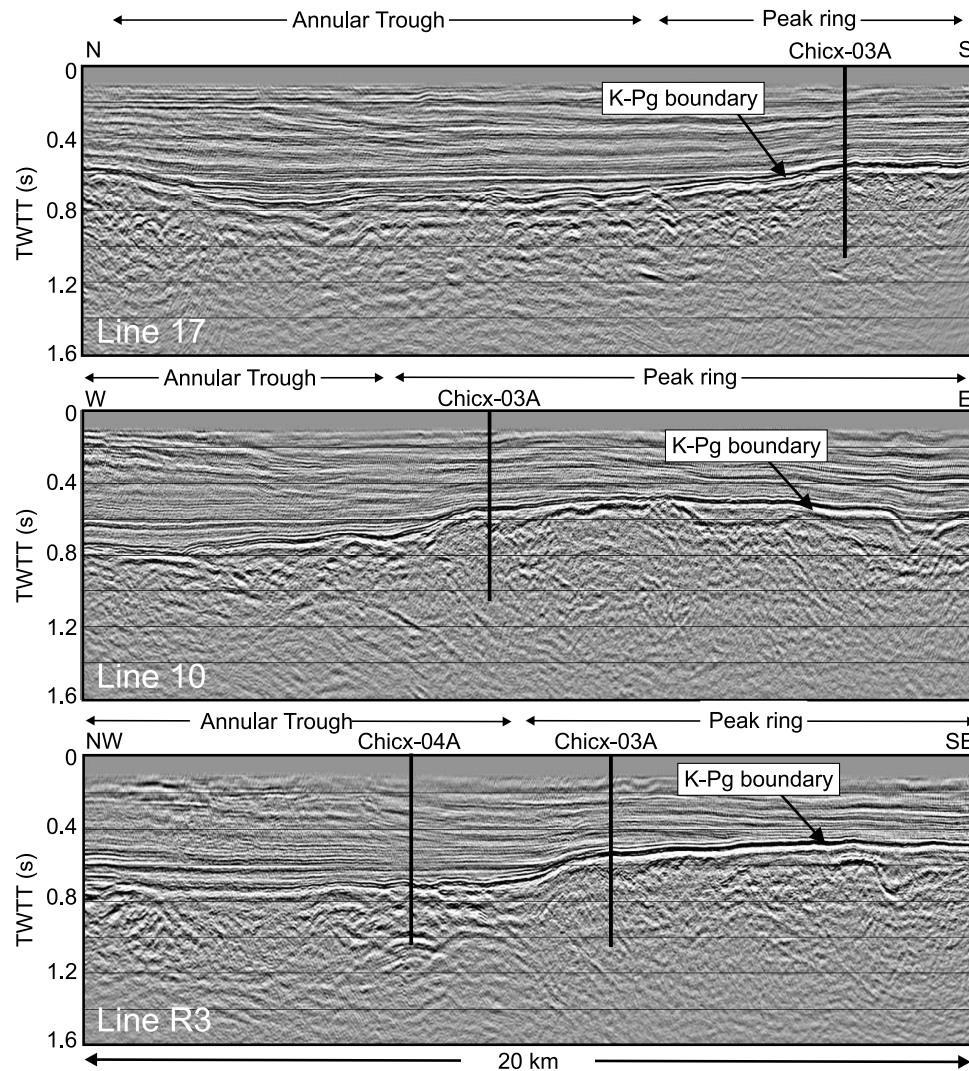
Figure 6. Migrated stacks of the seismic data for the three reflection profiles (lines 17, 10, and R3) used in this study (see Figure 3 for location). Chicx-03A and Chicx-04A show the location of two planned Integrated Ocean Drilling Program drill holes. The location of the K-Pg boundary has been located using onshore wells and is interpreted as the bright reflector that lies at the base of a suite of high-frequency reflectors [e.g., *Bell et al.*, 2004].

the seismic data. The input data were filtered using a minimum-phase Ormsby band-pass filter (5–14 Hz), with low- and high-cut ramps that were 5 and 10 Hz wide, respectively. An example of the seismic data input into the inversion is shown in Figure 7b; a mute has been used to remove the ground roll and later arrivals that are likely to contain *S* waves. These data were converted into the frequency domain using a Fourier transform, and data for five single frequencies (5, 6, 7, 8 and 10 Hz) were input into the inversion. Ten iterations were performed at each frequency. As an alternative to muting, different exponential weightings (0.2 s < τ < 1.2 s) were also explored, in which an exponential damping factor in the frequency domain is used to reduce the amplitude of later arrivals. A τ value of 0.8 was used for the inversions shown in Figure 9. Mutes and Tau values that passed more (higher τ) or less (lower τ) data

into the inversion tended to lead to a decrease or increase in the sharpness of our velocity images. The selected velocity model for line 17 (τ = 0.8), along with two other models obtained using different values of τ, are shown in Figure 10. Inversions that used either smaller time windows or smaller values of τ led to rougher velocity models, and tended to produce stronger velocity contrasts (see Figures 10b and 10e). In these models, some absolute velocities and changes in velocity lie outside the range expected from measurements on core in onshore boreholes [*Vermeesch and Morgan*, 2004; *Mayr et al.*, 2008]. Longer time windows and larger values of τ led to smoother models (see Figures 10c and 10f). The inversions in Figure 9 were chosen as they produced a reasonable fit between the calculated and observed data (see Figure 11), did not contain any obvious artifacts, and are geologically reasonable.
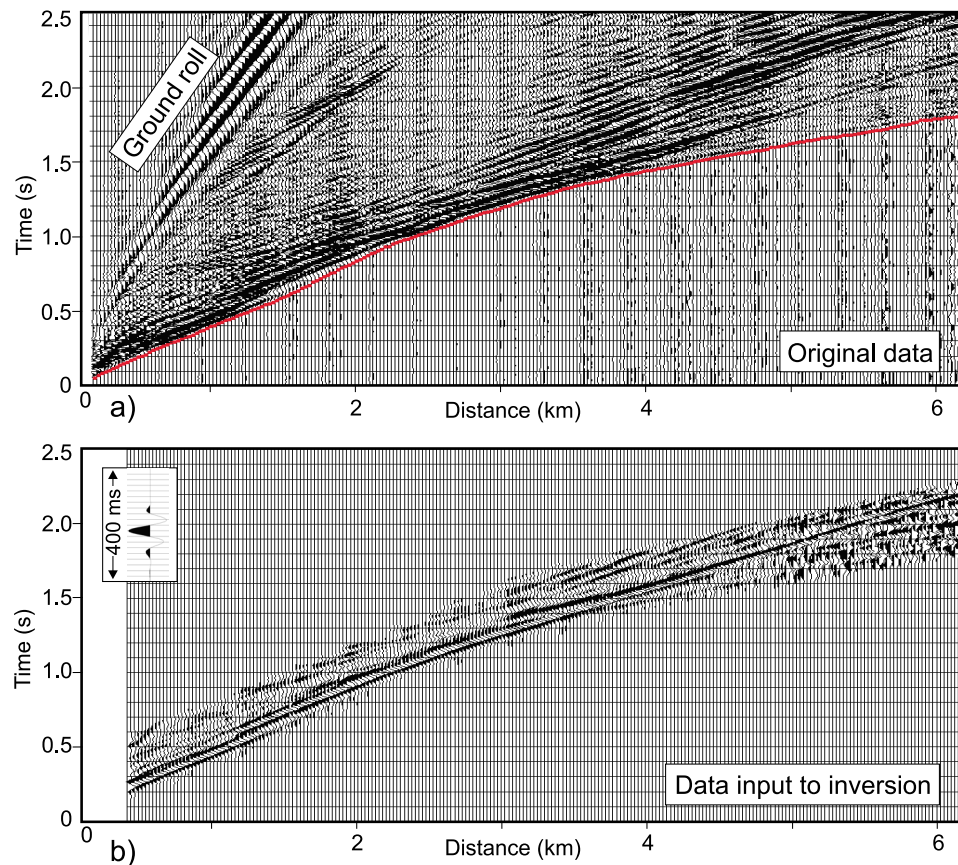
Figure 7. (a) Shot gather 154 from line 17 (see Figure 8 for location); red dashes are the first-arrival picks used for the FAST inversion. (b) The same shot gather processed in preparation for input to the full wavefield inversion. A mute has been applied to the near-offset data and later arrivals to remove the ground roll and secondary arrivals that are likely to contain S waves and multiples. The data have been band-pass filtered between 5 and 14 Hz. Inset is the source used for the full wavefield inversions.

[16] Approximately 30 inversions were run for each line and all showed essentially the same features: (1) that the peak ring is formed from relatively low-velocity material, (2) that there is a velocity inversion between the postimpact sediments and the uppermost peak-ring material, (3) that the lowermost Paleogene sediments in the annular trough have a relatively high velocity, (4) that some of the postimpact sediment packages are associated with slightly higher or lower velocities and the velocities track the deepening of these packages toward the center of the impact basin, and (5) that there are some high-velocity zones in the annular trough below the K-Pg boundary (see HVZ in Figure 9).

[17] We observe that, in all our models, velocities increase and decrease at about the same depths but the absolute velocities vary by a few hundred meters per second (see Figures 10a–10c). Figure 11 shows the match between the observed and synthetic wavefields. The data fit is particularly good at near and middle offsets (Figures 11a–11d). At far offsets, the match between the first-arrival travel times and early arrivals are reasonable but the wavefield match for later arrivals is poor (Figure 11e). This suggests that we can be confident about the overall character of the inverted velocity models but acknowledge that there is some uncertainty in absolute velocity values and depths, particularly in

deeper parts of the models that are constrained by the far-offset data.

4. Discussion

[18] The velocity models that were obtained by inverting for the full wavefield (Figure 9) resolve the fine-scale velocity structure within the peak ring down to depths of up to ~1.5 km. A surprising feature of these models is that the uppermost part of the peak ring exhibits a strong velocity inversion, with velocities changing from 3600 to 4000 m/s in the lowermost Paleogene to 3000–3200 m/s just below the K-Pg boundary. This low-velocity zone is ~100–200 m thick and velocities increase rapidly to >3600 m/s immediately below. On line 10 and R3, the velocity increase is associated with a low-frequency reflector (Figures 9b and 9c). The rest of the material that forms the peak ring has a fairly uniform velocity, with velocities of between 3900 and 4500 m/s. In the annular trough, there is a slightly smaller velocity inversion, from ~3800 m/s in the lowermost Paleogene to ~3500 m/s below the K-Pg boundary, and high-velocity zones are observed below depths of ~1300 m (HVZ in Figure 9). On all three lines, these high-velocity zones disappear near the outer edge of the peak ring, close to
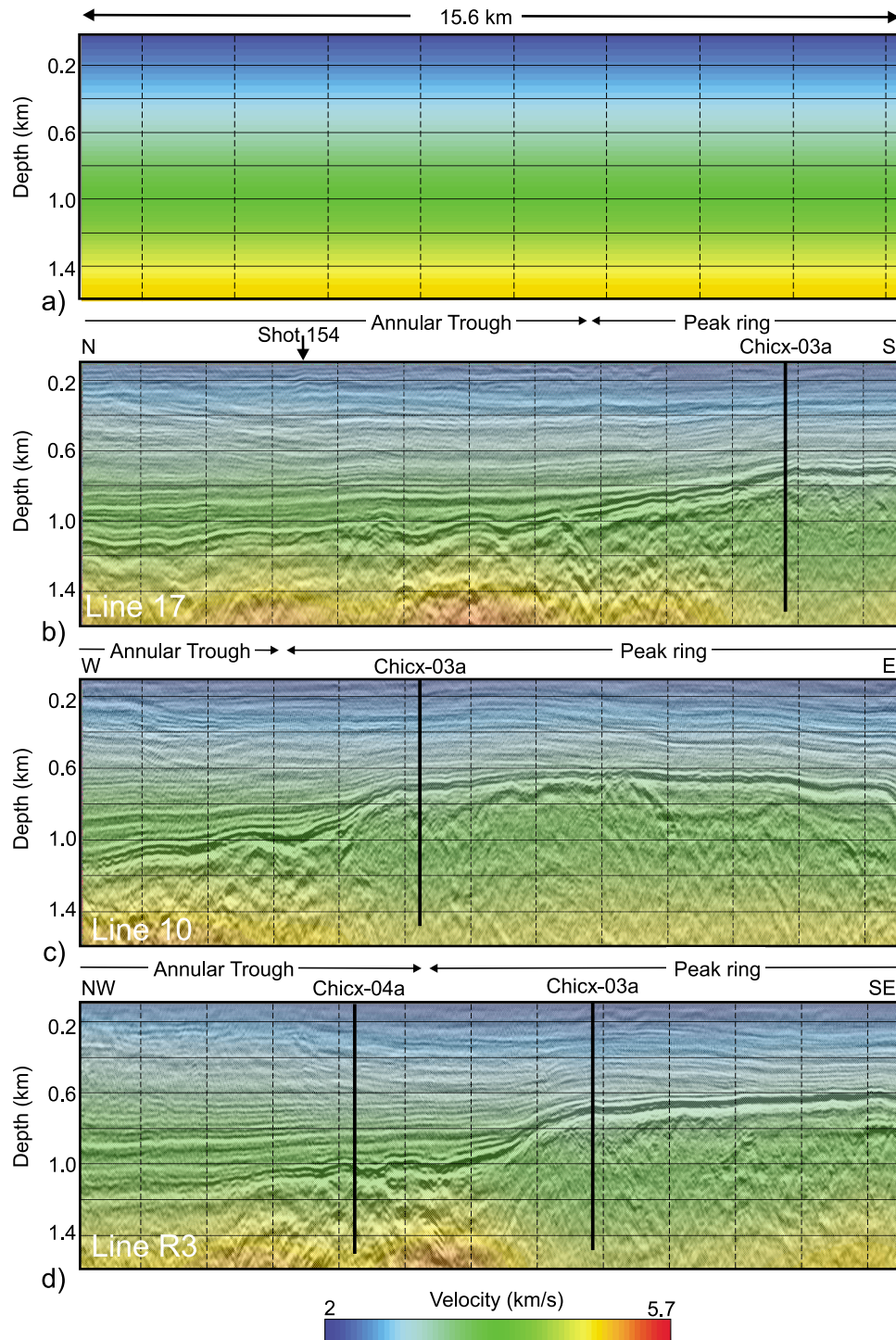
Figure 8. (a) Starting velocity model for the FAST inversions. Inverted velocity models and reflection stacks for (b) line 17, (c) line 10, and (d) line R3. Migrated reflection stacks are converted to depth using the inverted velocity model. Shot 154 marks the shot location of the example shot gather shown in Figure 7. The streamer is to the left of the shot.
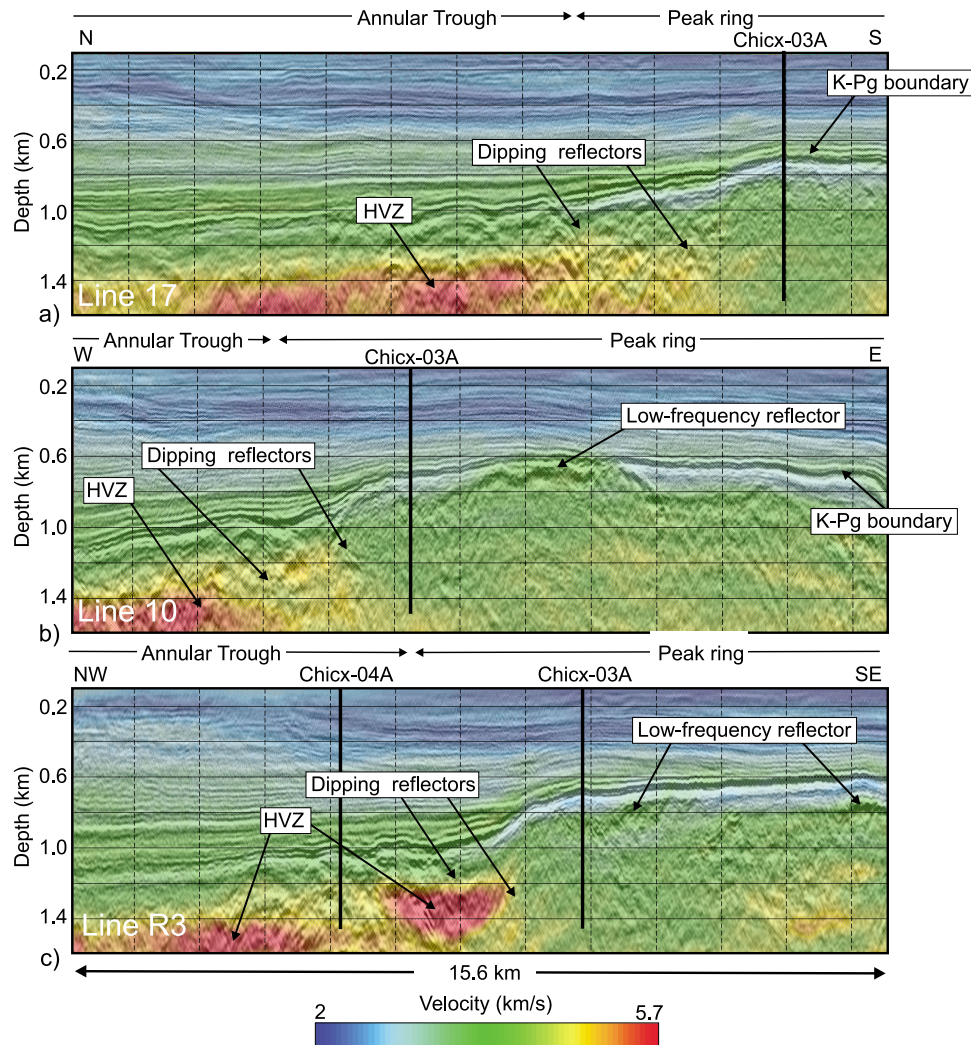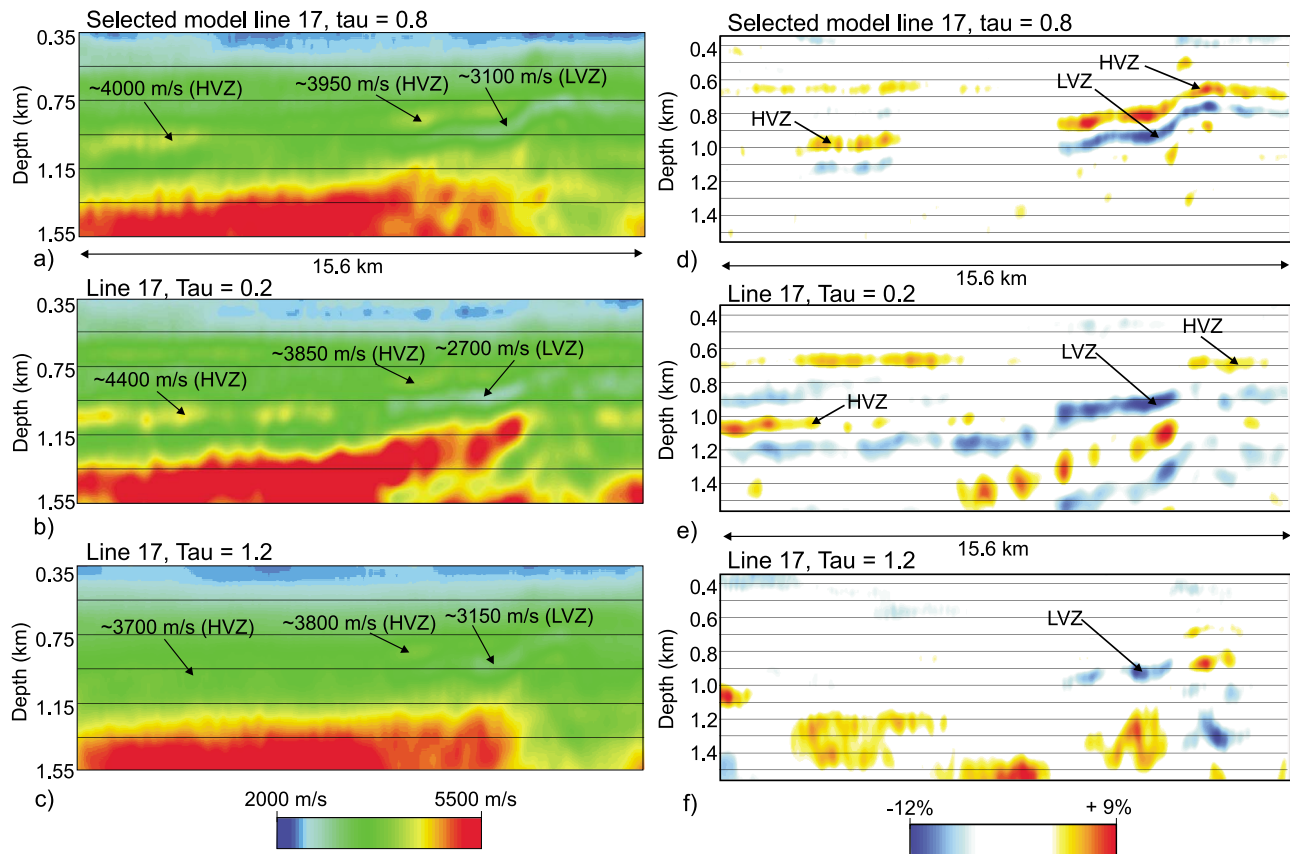
Figure 9. Selected full wavefield inverted velocity models and reflection stacks for (a) line 17, (b) line 10, and (c) line R3. Migrated reflection stacks are converted to depth using the inverted velocity model. The locations of the dipping reflectors have been extrapolated from deeper in the section, where the reflections are clearer (see Figure 2b). These velocity models cover the same horizontal distances and depths as those shown in Figure 8. HVZ indicates locations of high-velocity zones in rocks in the annular trough adjacent to the peak ring.

the location of the suite of inward dipping reflectors (see Figure 9).

[19] Here, we make a preliminary interpretation of these results, with some caution, as the velocity models are not considered to be perfect. In onshore wells located in the annular trough (Y6, Yax-1) and in the central basin (C1, S1), the lithologies immediately below the K-Pg boundary are allogenic impact breccias [*Hildebrand et al.*, 1991], with a relatively low velocity of ~3800 m/s [*Morgan et al.*, 2000]. Hence, we consider that the thin low-velocity layer at the top of the peak ring in our wavefield velocity models is most likely to be 100–200 m of highly porous allogenic impact breccias. In onshore wells S1 and C1, impact melt rocks were reached at ~1.4 km, and had measured velocities of >5.5 km/s. Hence, high-velocity zones that are located at similar depths in the central basin have been interpreted as impact melt rocks [*Morgan et al.*, 2000; *Barton et al.*, 2010]. Whether the high-velocity zones in the annular

trough are also impact melt rocks will be tested if proposed IODP drilling of hole Chicx-04A goes ahead as planned in 2013 (see Figures 3 and 9 for location).

[20] The lack of any high-velocity zones beneath the peak ring, and the relatively abrupt decrease in velocity at around the location of the dipping reflectors suggests that the rocks that form the peak ring are lithologically distinct from the surrounding rocks and that the dipping reflectors may well represent a boundary between two different lithologies. In Figure 4d we plot the maximum recorded shock pressures from a dynamic model of crater formation [*Collins et al.*, 2008a] and note that shock pressures appear to correlate with seismic velocity. The peak ring is formed from basement material that has been subjected to shock pressures of 10–50 GPa, whereas, the downthrown sediments (dashed line in Figure 4d) that underlie the peak ring are only weakly shocked (<5 GPa). In addition, the boundary between the weakly shocked sediments and highly shocked basement is

Figure 10. Full wavefield inverted velocity models for line 17 using (a) $\tau = 0.8$, (b) $\tau = 0.2$, and (c) $\tau = 1.2$. The velocity models all show similar features, but the absolute velocity values vary. This indicates that we can be reasonably confident about the structure of the velocity models but not the absolute velocity values. (d–f) Velocity perturbation (inverted minus starting velocity) for the models shown in Figures 10a–10c. The scale has been chosen to highlight perturbations that are greater than ±5%. HVZ is the high-velocity zone that corresponds to the lower Paleogene; LVZ is the low-velocity zone that forms the uppermost peak ring.

dipping and we speculate that this boundary might be the cause of the dipping reflectivity that is observed beneath the peak ring (compare Figures 2b and 4d).

[21] In the numerical model shown in Figure 4, the overturned basement rocks that form the peak ring have been subjected to such high plastic strain rates that the original configuration of the rock fragments would be lost [*Collins et al.*, 2008a]. We thus expect these rocks to be highly fractured and brecciated, which may explain why these rocks have a much lower velocity (3900–4500 m/s) than expected for this rock type. The basement rocks in this region have average refraction velocities of >5.5 km/s [*Christeson et al.*, 2001]. Physical property measurements on fractured rocks at terrestrial craters have reduced velocities and densities compared to their unfractured counterparts [see *Pilkington and Grieve*, 1992, Table 1]. Reduced densities are observed down to 5 km at the Siljan crater in Sweden and reductions in velocity at the Barringer crater are as high as 50% [*Pilkington and Grieve*, 1992]. It is possible that the low velocities are also caused by a metamorphic changes in the mineralogy (shock metamorphism). Observational and experimental data for a range of minerals show that there are phase changes associated with postshock decompression and that these changes affect their physical properties. The principal minerals in fragments of basement within the Chicxulub impact breccias are quartz and feldspar [*Kettrup and Deutsch*, 2003]. Feldspar and silicate minerals both show reductions in bulk density of 5–15% when subjected to high shock pressures [e.g., *Dworak*, 1969; *Ahrens et al.*, 1969; *Gibbons and Ahrens*, 1971; *Langenhorst and Deutsch*, 1994]. Hence, we conclude that fracturing and shock metamorphism may both contribute to the observed low velocities within the peak ring.

[22] The precise lithological character, structure and physical state of the lithologies that form the peak ring will be documented by the drilling of proposed IODP drill hole Chicx-03A (see Figure 9). The acquired core will allow us to ascertain the reason for the low velocities, within the peak ring, as well as the approximate depth of origin of the rocks that form the peak ring. These data will allow us to better constrain the kinematics of crater formation, as well as identify which internal rings at other large terrestrial craters are likely to be remnants of topographic peak rings.

[23] On Mercury, the Moon and Venus, peak rings show an increase in peak-ring/crater diameter ratio with increasing crater size [*Wood and Head*, 1976; *Head*, 1977; *Alexopoulos and McKinnon*, 1994], suggesting that outward collapse of the central uplift increases with impact size. Not
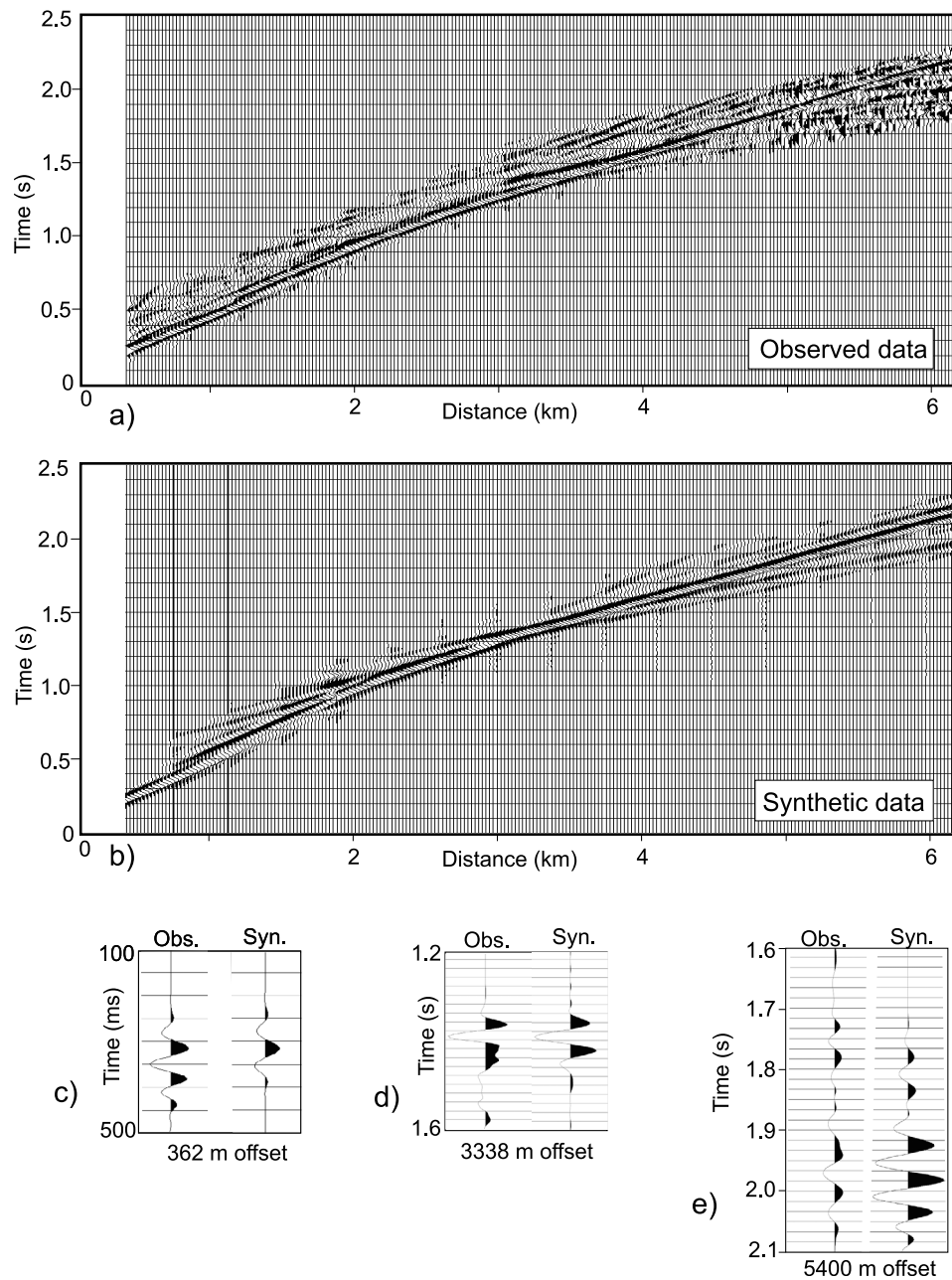
Figure 11. Comparison of (a) observed data and (b) synthetic data for shot 154 on line 17, with a close-up at (c) near-offset, (d) middle offset, and (e) far offset. The waveforms match reasonably well for near and middle offsets. At far offsets the first-arrival travel times and initial waveforms match reasonably well, but the match for later arrivals is quite poor.

all these internal rings, however, have the same morphological character. Most possess the classic annulus of rugged mountains (Figure 1), which may also be associated with a ridge-like feature (Figure 12a). Some (~10%), however, consist of only a circular ridge (Figure 12b) [*Alexopoulos and McKinnon*, 1994]. We suggest that these observations of annular rings on other planetary bodies are consistent with a model of peak ring formation that involves the interaction between an inwardly collapsing transient cavity rim and an outwardly collapsing structural uplift. Depending on the precise mechanics of this collapse, the structurally uplifted material may collapse across the terrace zone to form a peak ring (as appears to be the case at Chicxulub). Numerical models suggest that this scenario is most likely to occur when a large volume of material is highly weakened during impact (see Figure 13b) [*Wünnemann et al.*, 2005]. The final crater structure is comparable to Chicxulub (Figures 2 and 5) and is consistent with the majority of extraterrestrial peak ring craters. In contrast, the model in Figure 13a shows a case where the target is strong and a relatively smaller volume of material is weakened during crater formation. In this case, the inner edge of the terrace zone is observed to form an elevated ridge and this morphology is more consistent with observations at craters such
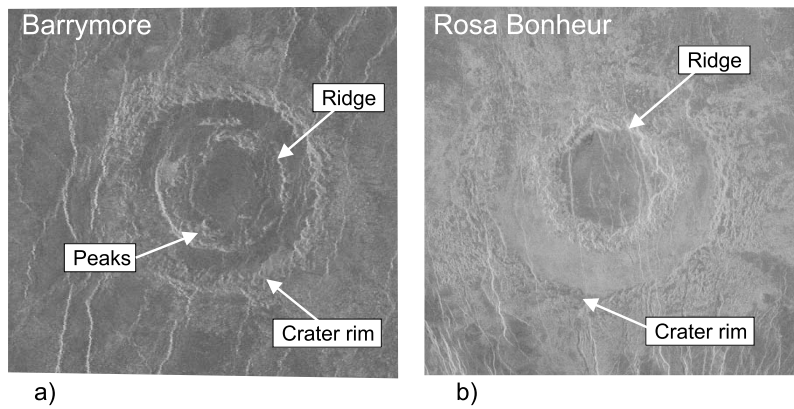
Figure 12. (a) Barrymore crater and (b) Rosa Bonheur crater on Venus are ~56 and ~102 km in diameter, respectively. The inner ring in both craters is formed from a ridge, and Barrymore also shows some peaks that are similar in character to those that form peak rings (e.g., Figure 1).

as Ries and Rosa Bonheur (Figure 12b). Although numerical models are nonunique and a range of parameterizations may lead to similar final crater structures, these models demonstrate that final crater morphology can be affected by target properties and the response of the target during cratering [*Collins et al.*, 2008b]. Additional complexity may occur in the case of a heterogeneous target, with modeling based on asymmetries at Chicxulub [*Collins et al.*, 2008a] suggesting that the thickness of the cover sequence and/or depth of

water in a hydrous target can affect the depth of the crater floor and morphology of the peak ring at different azimuths within a crater.

5. Summary

[24] The use of full wavefield techniques is increasing, as they can improve the resolution of subsurface velocity models. Models obtained from our full wavefield inversions

a)

b)
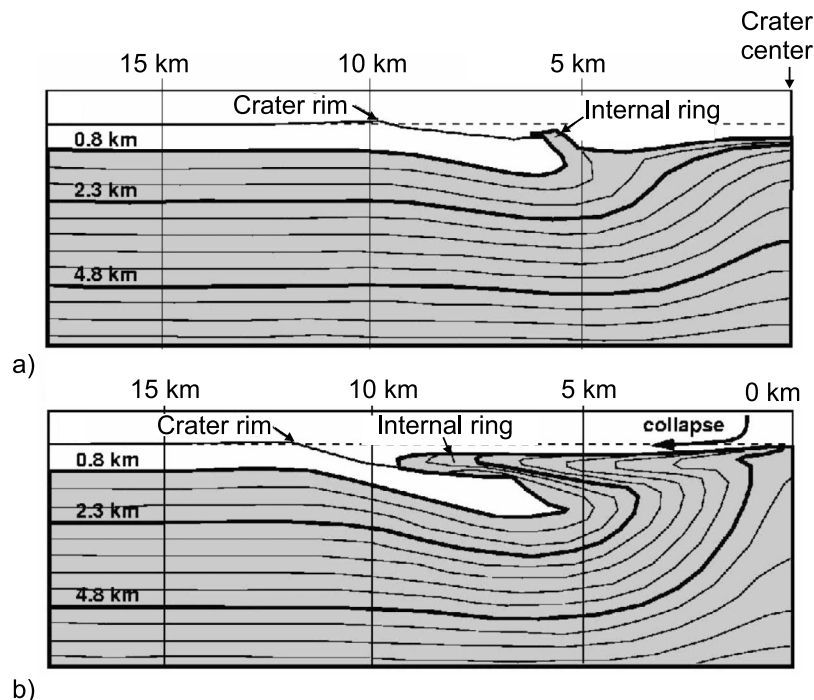
Figure 13. Two examples of numerical models of crater formation redrawn from *Wünnemann et al.* [2005]. (a) The uppermost target has a high strength, and a relatively small volume of target material undergoes moderate weakening. This leads to a final crater in which an annular ridge is formed from the inner edge of a terrace zone that has been overturned, and the annular trough is more elevated than the central basin. The final crater morphology is comparable to that at the Ries and Rosa Bonheur (Figure 12b) craters. (b) The uppermost target has a relatively low strength, and a large volume of target rocks are strongly weakened by the impact. The final crater structure is comparable to Chicxulub (Figure 5) and is consistent with the morphology of extraterrestrial peak ring craters (e.g., Figures 1 and 12a).

reveal the fine-scale velocity structure across the peak ring at Chicxulub. They confirm that the peak ring is formed from low-velocity material and show, for the first time, that a thin layer of low-velocity material forms the uppermost peak ring, and that there is an abrupt change in velocity between lithologies in the annular trough and peak ring. Low seismic velocities within the peak ring and adjacent annular trough show a correlation with predicted peak shock pressures in a dynamic model of crater formation. High shock pressures and the resultant reduction in density on decompression, high plastic strain rates, as well as phase changes due to shock metamorphism, may be responsible for the unusually low velocities observed within the peak ring at Chicxulub.

References

Ahrens, T. J., C. F. Petersen, and J. T. Rosenburg (1969), Shock compression of feldspars, *J. Geophys. Res.*, *74*, 2727–2746, doi:10.1029/JB074i010p02727.

Alexopoulos, J. S., and W. B. McKinnon (1994), Large impact craters and basins on Venus, with implications for ring mechanics on the terrestrial planets, *Spec. Pap. Geol. Soc. Am.*, *293*, 29–50.

Barton, P. J., R. A. F. Grieve, J. V. Morgan, A. T. Surendra, P. M. Vermeesch, G. L. Christeson, S. P. S. Gulick, and M. R. Warner (2010), Seismic images of Chicxulub impact melt sheet and comparison with the Sudbury structure, *Spec. Pap. Geol. Soc. Am.*, *465*, 103–113, doi:10.1130/2010.2465(07).

Bell, C., J. V. Morgan, G. J. Hampson, and B. Trudgill (2004), Stratigraphic and sedimentological observations from seismic data across the Chicxulub impact basin, *Meteorit. Planet. Sci.*, *39*, 1089–1098, doi:10.1111/j.1945-5100.2004.tb01130.x.

Brenders, A. J., and R. G. Pratt (2007), Full waveform tomography for lithospheric imaging: Results from a blind test in a realistic crustal model, *Geophys. J. Int.*, *168*, 133–151, doi:10.1111/j.1365-246X.2006.03156.x.

Bussey, D. B. J., and P. D. Spudis (1997), Compositional analysis of the Orientale basin using full resolution Clementine data, *Geophys. Res. Lett.*, *24*, 445–448, doi:10.1029/97GL00178.

Christeson, G. L., R. T. Buffler, and Y. Nakamura (1999), Upper crustal structure of the Chicxulub impact crater from wide-angle ocean bottom seismograph data, *Spec. Pap. Geol. Soc. Am.*, *339*, 291–298, doi:10.1130/0-8137-2339-6.291.

Christeson, G. L., Y. Nakamura, R. T. Buffler, J. Morgan, and M. Warner (2001), Deep crustal structure of the Chicxulub impact crater, *J. Geophys. Res.*, *106*, 21,751–21,769, doi:10.1029/2001JB000337.

Collins, G. S., H. J. Melosh, J. V. Morgan, and M. R. Warner (2002), Hydrocode simulations of Chicxulub crater collapse and peak-ring formation, *Icarus*, *157*, 24–33, doi:10.1006/icar.2002.6822.

Collins, G. S., J. Morgan, P. Barton, G. L. Christeson, S. Gulick, J. Urrutia-Fucugauchi, M. Warner, and K. Wünnemann (2008a), Dynamic modeling suggests asymmetries in the Chicxulub crater are caused by target heterogeneity, *Earth Planet. Sci. Lett.*, *270*, 221–230, doi:10.1016/j.epsl.2008.03.032.

Collins, G. S., T. Kenkmann, G. R. Osinski, and K. Wunnemann (2008b), Mid-sized complex crater formation in mixed crystalline-sedimentary targets: Insight from modeling and observation, *Meteorit. Planet. Sci.*, *43*, 1955–1977, doi:10.1111/j.1945-5100.2008.tb00655.x.

Dworak, U. (1969), Stoßwellenmetamorphose des Anorthosits vom Manicouagan Krater, Québec, Canada, *Contrib. Mineral. Petrol.*, *24*, 306–347, doi:10.1007/BF00371273.

Gibbons, R. V., and T. J. Ahrens (1971), Shock metamorphism of silicate glasses, *J. Geophys. Res.*, *76*, 5489–5498, doi:10.1029/JB076i023p05489.

Grieve, R. A. F., P. B. Robertson, and M. R. Dence (1981), Constraints on the formation of ring impact structures, based on terrestrial data, *Proc. Lunar Planet. Sci. Conf.*, *12th*, 37–57.

Grieve, R. A. F., U. Reimold, J. V. Morgan, U. Riller, and M. Pilkington (2008), Observations and interpretations at Vredefort, Sudbury and Chicxulub: Towards a composite model of a terrestrial impact basin, *Meteorit. Planet. Sci.*, *43*, 855–882, doi:10.1111/j.1945-5100.2008.tb01086.x.

Gulick, S. P. S., et al. (2008), Importance of pre-impact crustal structure for the asymmetry of the Chicxulub impact crater, *Nat. Geosci.*, *1*, 131–135, doi:10.1038/ngeo103.

Head, J. W. (1977), Origin of rings in lunar multi-ringed basins: Evidence from morphology and ring spacing, in *Impact and Explosion Cratering*, edited by D. J. Roddy, R. O. Pepin, and R. B. Merrill, pp. 563–573, Pergamon, New York.

Hildebrand, A. R., G. T. Penfield, D. A. Kring, M. Pilkington, A. Camargo-Zanoguera, S. B. Jacobsen, and W. V. Boynton (1991), Chicxulub crater: A possible Cretaceous/Tertiary boundary impact crater on the Yucatán Peninsula, Mexico, *Geology*, *19*, 867–871, doi:10.1130/0091-7613(1991)019<0867:CCAPCT>2.3.CO;2.

Ivanov, B. A. (2005), Numerical modeling of the largest terrestrial meteorite craters, *Sol. Syst. Res.*, *39*, 381–409, doi:10.1007/s11208-005-0051-0.

Kettrup, B., and A. Deutsch (2003), Geochemical variability of the Yucatan basement: Constraints from crystalline clasts in Chicxulub impactites, *Meteorit. Planet. Sci.*, *38*, 1079–1092, doi:10.1111/j.1945-5100.2003.tb00299.x.

Langenhorst, F., and A. Deutsch (1994), Shock experiments on pre-heated α- and β-quartz: 1. Optical and density data, *Earth Planet. Sci. Lett.*, *125*, 407–420, doi:10.1016/0012-821X(94)90229-1.

Mayr, S. I., A. Wittmann, H. Burkhardt, Y. Popov, R. Romushkevich, I. Bayuk, P. Heidinger, and H. Wilhelm (2008), Integrated interpretation of physical properties of rocks of the borehole Yaxcopoil-1 (Chicxulub impact structure), *J. Geophys. Res.*, *113*, B07201, doi:10.1029/2007JB005420.

Melosh, H. J. (1989), *Impact Cratering: A Geological Process*, 245 pp., Oxford Univ. Press, New York.s

Morgan, J., et al. (1997), Size and morphology of the Chicxulub impact crater, *Nature*, *390*, 472–476, doi:10.1038/37291.

Morgan, J., M. R. Warner, G. S. Collins, H. J. Melosh, and G. L. Christeson (2000), Peak-ring formation in large impact craters: Geophysical constraints from Chicxulub, *Earth Planet. Sci. Lett.*, *183*, 347–354, doi:10.1016/S0012-821X(00)00307-1.

Pilkington, M., and R. A. F. Grieve (1992), The geophysical signature of terrestrial impact craters, *Rev. Geophys.*, *30*, 161–181, doi:10.1029/92RG00192.

Pilkington, M., A. R. Hildebrand, and C. Ortiz-Aleman (1994), Gravity and magnetic field modeling and structure of the Chicxulub crater, Mexico, *J. Geophys. Res.*, *99*, 13,147–13,162, doi:10.1029/94JE01089.

Pratt, R. G. (1999), Seismic waveform inversion in the frequency domain, part I: Theory and verification in a physical scale model, *Geophysics*, *64*, 888–901, doi:10.1190/1.1444597.

Pratt, R. G., and M. H. Worthington (1988), The application of diffraction tomography to cross-hole seismic data, *Geophysics*, *53*, 1284–1294, doi:10.1190/1.1442406.

Schulte, P., et al. (2010), The Chicxulub asteroid impact and mass extinction at the Cretaceous-Paleogene boundary, *Science*, *327*, 1214–1218, doi:10.1126/science.1177265.

Senft, L. E., and S. T. Stewart (2009), Dynamic fault weakening and the formation of large impact craters, *Earth Planet. Sci. Lett.*, *287*, 471–482, doi:10.1016/j.epsl.2009.08.033.

Sirgue, L. (2003), Inversion de la forme d'onde dans le domaine fréquentiel de données sismiques grands offsets, Ph.D. thesis, École Normale Super. de Paris, Paris.

Sirgue, L., and R. G. Pratt (2004), Efficient waveform inversion and imaging: A strategy for selecting temporal frequencies, *Geophysics*, *69*, 231–248, doi:10.1190/1.1649391.

Sirgue, L., O. I. Barkved, J. Dellinger, J. Etgen, U. Albertin, and J. H. Kommedal (2010), Full waveform inversion: The next leap forward in imaging at Valhall, *First Break*, *28*, 65–70.

Takougang, E. M. T., and A. J. Calvert (2011), Applications of waveform tomography to marine seismic reflection data from the Queen Charlotte Basin of western Canada, *Geophysics*, *76*, B55, doi:10.1190/1.3553478.

Vermeesch, P. M., and J. V. Morgan (2004), Structure of Chicxulub: Where do we stand?, *Meteorit. Planet. Sci.*, *39*, 1019–1034, doi:10.1111/j.1945-5100.2004.tb01127.x.

Vermeesch, P. M., and J. V. Morgan (2008), Structural uplift beneath the Chicxulub impact structure, *J. Geophys. Res.*, *113*, B07103, doi:10.1029/2007JB005393.

Williamson, P. (1991), A guide to the limits of the resolution imposed by scattering in ray tomography, *Geophysics*, *56*, 202–208, doi:10.1190/1.1443032.

Wood, C. A., and J. W. Head (1976), Comparison of impact basins on mercury, Mars and the Moon, *Proc. Lunar Planet. Sci. Conf.*, *7th*, 3629–3651.

Wu, R., and M. N. Toksöz (1987), Diffraction tomography and multi-source holography applied to seismic imaging, *Geophysics*, *52*, 11–25, doi:10.1190/1.1442237.

Wünnemann, K., J. V. Morgan, and H. Joedicke (2005), Is Ries Crater typical for its size? An analysis based upon old and new geophysical data and numerical modeling, in *Spec. Pap. Geol. Soc. Am.*, *384*, 67–83, doi:10.1130/0-8137-2384-1.67.

Zelt, C. A. (1999), Modeling strategies and model assessment for wide-angle seismic traveltime data, *Geophys. J. Int.*, *139*, 183–204, doi:10.1046/j.1365-246X.1999.00934.x.

Zelt, C. A., and P. J. Barton (1998), Three-dimensional seismic refraction tomography: A comparison of two methods applied to data from the Faeroe Basin, *J. Geophys. Res.*, *103*, 7187–7210, doi:10.1029/97JB03536.

P. J. Barton, Department of Earth Sciences, University of Cambridge, Cambridge CB3 0EZ, UK.

G. L. Christeson and S. P. S. Gulick, Jackson School of Geosciences, University of Texas Institute for Geophysics, Austin, TX 78758, USA.

G. S. Collins, J. V. Morgan, and M. R. Warner, Department of Earth Science and Engineering, Imperial College London, South Kensington Campus, London SW7 2AZ, UK. (j.v.morgan@imperial.ac.uk)

R. A. F. Grieve, Department of Earth Sciences, University of Western Ontario, London, ON N6A 5B7, Canada.